Formation, growth and dissociation of He bubbles in Al2O3

van Huis, MA; van Veen, A; Labohm, F; Fedorov, AV; Schut, H; Kooi, BJ; De Hosson, JTM

Link to publication in University of Groningen/UMCG research database

Formation, growth and dissociation of He bubbles in Al_2O_3

M.A. van Huis [a,*], A. van Veen [a], F. Labohm [a], A.V. Fedorov [a], H. Schut [a],
B.J. Kooi [b], J.Th.M. De Hosson [b]

[a] *Interfaculty Reactor Institute, Delft University of Technology, Mekelweg 15, 2629 JB Delft, The Netherlands*
[b] *Materials Science Center, University of Groningen, Nijenborgh 4, 9749 AG Groningen, The Netherlands*

Abstract

The formation and dissociation of helium bubbles and helium desorption are investigated in sapphire $Al_2O_3(0\,0\,0\,1)$ implanted with 30 keV He ions to four different doses of 0.1, 0.3, 1.0 and 2.0×10^{16} ions cm^{-2}. The samples were annealed isochronally up to 1850 K in steps of 100 K. The techniques of Doppler broadening positron beam analysis (PBA) and neutron depth profiling (NDP) were used to investigate defect evolution and helium retention, respectively, during the annealing procedure. It was observed that the maximum bubble volume is found after 1250 K annealing, after which a process of bubble shrinkage sets in. Cross-sectional transmission electron microscopy (XTEM) was performed on the sample that was implanted with the highest-dose (2.0×10^{16} He ions cm^{-2}) after annealing at 1250 K. It was found that the bubbles are shaped as discs lying parallel with the surface and that the average bubble size is 5.5 nm. In all samples, helium is released mainly at a temperature of 1750 K. The desorption curves were analyzed by means of a permeation model. The activation energy for permeation was found as 4.0 eV.
© 2003 Elsevier B.V. All rights reserved.

PACS: 61.46. + w; 61.80.−x; 68.43.Vx; 68.55.Ln
Keywords: Helium; Bubbles; Sapphire; Ion implantation; Desorption

1. Introduction

The interest in the behavior of helium in Al_2O_3 arises from two applications. First, Al_2O_3 is a candidate host matrix for the transmutation of actinides generated in nuclear reactor fuels [1]. Alpha decay of actinides introduces helium atoms into the Al_2O_3 matrix that interact with radiation damage defects. It is therefore of interest to investigate the relevant activation energies for dissociation of helium from defects. Second, Al_2O_3 is a popular host material for the generation of linear and non-linear optical properties by introducing metallic or semiconductor nanoclusters [2,3]. Ion implantation of inert gas atoms such as He can improve the understanding of defect evolution in ion implanted Al_2O_3, which is also of importance to the formation of metal or semiconductor nanoclusters. Although various studies have been performed on He^+ implanted Al_2O_3 [4–6], release of helium from monocrystalline alumina has never been reported. In this work, helium desorption and the helium atomic depth distribution is monitored by means of neutron depth profiling (NDP). The defect evolution in the ion

* Corresponding author. Tel.: +31-152-781-612; fax: +31-152-786-422.
E-mail address: vanhuis@iri.tudelft.nl (M.A. van Huis).

implanted samples is investigated by means of positron beam analysis (PBA). Positrons are very sensitive tools to probe vacancy-type defects and the formation of bubbles [7]. Both techniques are non-destructive and depth-sensitive. Cross-sectional transmission electron microscopy (XTEM) was employed to determine the size and concentration of He bubbles. These parameters are required for application of a permeation model to the desorption data.

2. Experimental

Four epi-polished $Al_2O_3(0\,0\,0\,1)$ single crystals of size $10 \times 10 \times 1$ mm^3 were implanted at room temperature with 30 keV ^{3}He ions to four different doses of 0.1, 0.3, 1.0 and 2.0×10^{16} ions cm^{-2}. The samples were isochronally annealed in ambient air during a period of 0.5 h at temperatures varying from 550 to 1850 K in steps of 100 K. The inaccuracy in the annealing temperature is approximately 20 K. After ion implantation and after each annealing step, the sample was cooled down and the evolution of ion implantation defects was monitored by means of Doppler broadening positron beam analysis (PBA) [8] and neutron depth profiling (NDP) [9]. The PBA set-up uses a 0–30 keV monoenergetic positron beam. This corresponds to a mean positron implantation depth of 0–2.0 µm, which allows depth-resolved monitoring of the defect evolution. The NDP technique uses the ^{3}He(n,p)^{3}H nuclear reaction in order to determine the total amount and the depth distribution of He atoms present in the sample. The inaccuracy in the absolute ^{3}He content is in general 7% but larger for low doses ($<10^{15}$ ions cm^{-2}). Finally, XTEM was applied to a fifth sample that received the same treatment as the sample implanted with the highest He dose (2.0×10^{16} ions cm^{-2}), but where the annealing sequence was stopped after the 1250 K annealing step. This temperature corresponds to the largest bubble volume as observed by means of PBA. The TEM analysis was performed with a JEOL 4000 EX/II electron microscope operating at 400 keV (point-to-point resolution 0.165 nm). The specimen preparation is discussed elsewhere [10].

3. Results and discussion

3.1. PBA results: defect evolution

Fig. 1 shows the S parameter as a function of positron implantation energy for the high-dose (2.0×10^{16} He ions cm^{-2}) implanted sample. The S (shape) parameter is deduced from the Doppler broadening of the 511 keV positron annihilation peak and indicates the relative contribution of positron annihilation with valence and conduction electrons [8]. A high value of the S parameter indicates the presence of vacancies and vacancy clusters. If the vacancy clusters are larger than about 2 nm, the S parameter can further increase due to the formation of positronium (Ps) inside the voids. Positronium is a hydrogen-like bound state of a positron and an electron that leads to a strong increase in the S parameter [8]. The presence of helium inside the vacancy clusters is known to
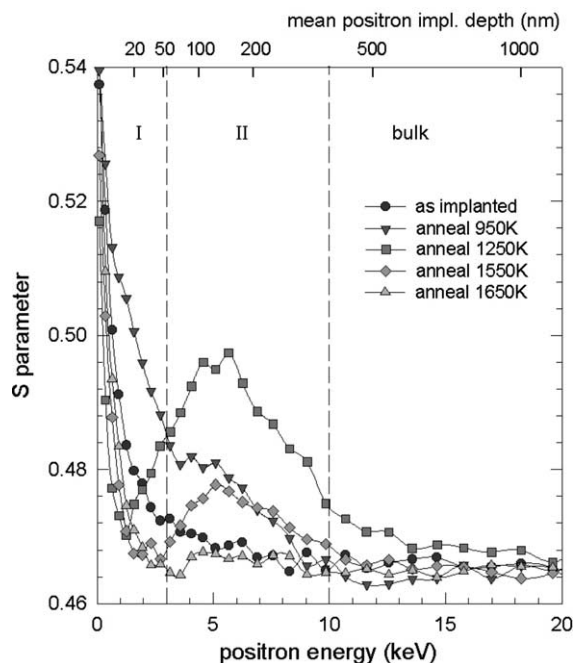

Fig. 1. S parameter versus positron implantation energy for the high-dose (2.0×10^{16} cm^{-2}) ^{3}He implanted sample after implantation and after the indicated annealing temperatures. Lines are drawn to guide the eye. The mean positron implantation depth is displayed at the top of the figure.

suppress the formation of Ps. This was found, e.g., for the case of silicon where Ps formation in empty and in helium-filled voids was compared [11,12]. Fig. 1 shows the S parameter (indicator of open volume) as a function of positron implantation energy, after ion implantation and after several annealing steps. The positron implantation energy along the abscissa of Fig. 1 corresponds to a mean positron implantation depth that is indicated at the top of the figure. For the discussion, we use a two-layer model: there is a top layer that contains mainly ion implantation damage (layer I in Fig. 1) and a layer containing mainly He-related defects (layer II). The layers indicated in the figure cannot be directly related to the depth scale given on top of the figure. Due to the width of the positron implantation profile and positron diffusion processes, a thin layer of defects will appear much broader in the S parameter curve. We will now discuss the defect evolution using Fig. 1.

1. After implantation, the S parameter of layers I and II increase slightly with respect to the S parameter of the Al_2O_3 bulk (positron energy >15 keV). Al_2O_3 is a Schottky material where the interstitials are mobile at room temperature and vacancies are not [13]. Thus the interstitials from Frenkel defects created by the implantation will either recombine with vacancies or move to the surface (so that the Frenkel defects turn into Schottky defects). Therefore, mainly vacancies and divacancies present after implantation (and 'annealing' at room temperature) contribute to the slight increase of the S parameter.
2. Annealing at 550–950 K: The S parameter in layers I and II increases. This means that larger vacancy clusters are formed because vacancies created by the ion implantation agglomerate.
3. Annealing at 950–1250 K: The S parameter decreases in layer I, indicating that the vacancy-type defects in layer I dissociate. Simultaneously, the S parameter increases considerably in layer II, showing that He bubbles are formed. The maximum bubble volume is found after annealing at 1250 K.
4. Annealing at 1250–1850 K: The S parameter in layer II decreases and reaches the Al_2O_3 bulk

value after annealing at 1650 K. Apparently the He bubbles undergo shrinkage and are not observable anymore after annealing at 1650 K. Simultaneously, the NDP results that will be discussed below show that 70% of the implanted He is still present in the sample at this temperature.

The results indicate that the PBA technique is not able to detect the He bubbles after annealing at 1650 K. This is most likely caused by the high pressure of He in the bubbles, which suppresses the formation of positronium. The observation of strong bubble shrinkage in combination with helium retention in the temperature interval 1250–1650 K is a situation that is very different to He release in MgO [7,14] where nanometer-sized voids are stable even when all He has been released. The low dose implanted samples ($<5 \times 10^{15}$ He cm^{-2}) showed a similar defect evolution, although the detected bubble volume did not develop as strongly as for the high-dose implanted samples.

3.2. XTEM results

In order to obtain information on the average size and the size distribution of the He bubbles, a specimen was prepared from the high-dose sample (2×10^{16} He cm^{-2}) after the 1250 K annealing step. This temperature was chosen because the S parameter is the highest after annealing at this temperature, indicating a maximum in bubble volume. An overview image is shown in Fig. 2. The ion implantation layer is clearly observable as a band with dark contrast at a depth of 230–340 nm below the surface. At shallower depth, there is a low density of large He bubbles. In this area, the number of displacements per atom (dpa) is lower than in the ion implantation layer. Therefore, monovacancies and He-vacancy defect complexes travel large distances before clustering with other vacancy-type defects. The result is the formation of fewer bubbles that are larger in size. The PBA results (Fig. 1) seem to disagree with the TEM results (Fig. 2) on the depth of the ion implantation layer. The peak in the S parameter is found at a positron implantation energy corresponding to a depth of 100–200 nm, while the depth of the
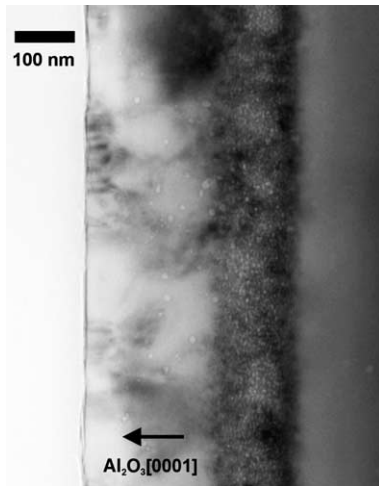
Fig. 2. Bright-field XTEM image showing the surface of the specimen and the ion implantation layer at a depth of 230–340 nm.

Fig. 3. Bright-field XTEM image in underfocus condition showing He bubbles in Al_2O_3. The average bubble size and the number of bubbles per unit of surface area are deduced from this image (see text).

helium implantation layer is 230–340 nm as observed by means of TEM. The reason for this difference is that the peak in the S parameter curve does not correspond exactly to the helium implantation layer. As is clear from Fig. 2, there are quite large bubbles present at a depth of 100–200 nm, shallower than the ion implantation layer. As a first approximation, the pressure in the bubbles is inversely proportional to the size of the bubbles, $p = 2\gamma/R$ with R the radius of the bubbles [15]. Therefore, the He pressure is lower in the large bubbles, so that efficient positronium formation occurs, which contributes strongly to the high S parameter at this depth [11]. Simultaneously, positronium is not or less formed in the smaller, higher-pressurized He bubbles in the ion implantation layer. Therefore, the peak present in the S parameter curve in Fig. 1 does not correspond to the ion implantation layer itself.

Fig. 3 shows a magnification of the bubbles in the implantation layer in a thin part of the specimen. Considering that the image is a cross-section, it is clear that the bubbles are shaped as discs lying parallel to the surface. The small bubbles are quite flat, the large bubbles are more three-dimensionally shaped and sizes vary from a few to 16 nm. The reason that the bubbles are shaped as discs rather than as bubbles can have two causes. First,
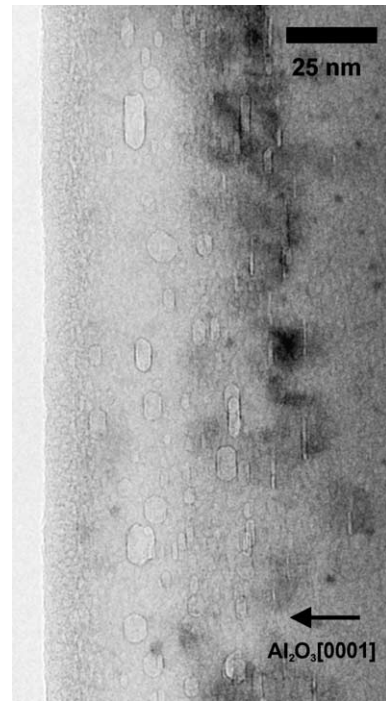
the interface energy can be different for different facets. So if the $Al_2O_3\{0\,0\,0\,1\}$ surfaces have very low surface energy, these facets will be relatively large. Second, probably there are stresses present in the material because of the ion implantation, which might also influence the energy balance to induce a non-spherical shape of the bubbles. The volume of 52 bubbles in Fig. 3 was calculated taking account for the disc-like shape of the bubbles. With the size defined as the cube root of the bubble volume, the average size was determined as 5.5 nm. Therefore, the average bubble volume, V_b is 165 nm^3. Here it should be remarked that large bubbles are much easier to observe than small bubbles, which leads to an overestimation of the average bubble volume. The bubble concentration inside the ion implantation layer was also estimated from Fig. 3, at 1.4×10^{17} bubbles cm^{-3}. Here it was assumed that the local TEM specimen thickness of the area displayed in Fig. 3 is 30 nm

thick. Since the ion implantation layer is 110 nm thick in depth (Fig. 2), the planar bubble concentration in the sample is 1.54×10^{12} bubbles cm^{-2}. Now that the bubble concentration and the bubble size are known, the number of vacancies constituting the bubbles can be calculated. Using the numbers above and the atomic density of Al_2O_3 (1.2×10^{23} atoms cm^{-3}), the total number of vacancies in the sample is found as 3.0×10^{16} cm^{-2}. Considering that the implanted He dose was 2×10^{16} cm^{-2}, this means that there are 1.5 displacements per He ion that have survived after annealing at 1250 K. This is a very reasonable value from an empirical point of view. It should be realized that all the bubbles displayed in Figs. 2 and 3 are still filled with helium. This is proven by the NDP/desorption results that are presented below.

3.3. NDP: Helium desorption

Fig. 4 shows the normalized retained He content in the samples as a function of annealing temperature, as measured by means of NDP. All four samples (high and low dose) follow the same trend. The largest decrease in helium content is observed after the 1750 K annealing step for all four doses. However, the desorption process is slower for the low dose ($<10^{16}$ cm^{-2}) implanted samples when compared to the samples implanted with higher He doses. We will now discuss the experimental desorption results using a permeation model. When dissolving the helium is the rate-determining step, the helium release from the layer of gas bubbles can be modelled as a quasi-stationary flow of gas. This flow is sustained by the gradient that exists from the equilibrium concentration $c_{He,eq}$ of dissolved gas near the cavity layer to the zero concentration near the external surface [15–17].

$$\frac{dN_{He}}{dt} = -D\frac{dc_{He}}{dx} = -D\frac{c_{He,eq}}{L}. \quad (1)$$

Here dN_{He}/dt is the flow rate of helium atoms per unit area in $m^{-2}\,s^{-1}$, c_{He} is the concentration of helium atoms, x is the depth in the sample and L the thickness of the Al_2O_3 top layer (230 nm). D is the helium diffusivity in $m^2\,s^{-1}$. Refs. [15–17] give
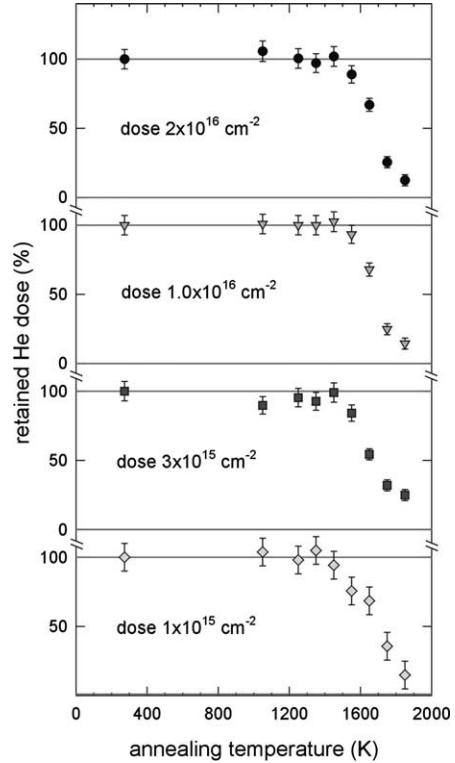

Fig. 4. Normalized concentration of He in the sample as observed by NDP, after implantation and during the annealing treatment for the four indicated implantation doses.

expressions for the diffusivity and the equilibrium concentration of helium for the case of a dense bubble layer with gas at low helium pressure and a planar configuration. Substitution of these equations in Eq. (1) and integration with respect to time yields the following expression for the number of retained helium atoms:

$$\frac{N_{He}}{N_0} = e^{-ft},$$

$$f = \frac{\lambda^2\omega}{12\pi L}\frac{c_{Al_2O_3}}{d_c}\left(\frac{2\pi\hbar^2}{mkT}\right)^{3/2}\left(\frac{kT}{\hbar\omega}\right)^3 e^{-E_{perm}/kT}. \quad (2)$$

Here N_{He} is the number of retained helium atoms, N_0 is the initial number of helium atoms, t is the period of time during which the permeation occurs (1800 s), λ is the jumping distance between two interstitial sites (2.0 Å), ω is a fundamental attempt frequency taken as the Debye frequency 10^{13} s^{-1}, $c_{Al_2O_3}$ the atomic concentration of sapphire

Al_2O_3 (1.18×10^{29} atoms m^{-3}), m the mass of the ^{3}He atom in kg, k the Boltzmann constant (8.62×10^{-5} eV K^{-1}) and T the temperature in K. The permeation energy E_{perm} is defined as the sum of the helium solution energy and the helium migration energy. Please refer to the references mentioned above for a more extensive discussion. The effective thickness d_c is the total bubble volume per unit area and can be written

$$d_c = N_b V_b / A, \tag{3}$$

assuming that all bubbles have the same diameter. Here N_b is the number of helium bubbles, V_b the bubble volume and A the area of the bubble layer (1.0 cm^2). In the previous subsection, N_b and V_b were calculated from the TEM analysis as 1.54×10^{12} and 165 nm^3, respectively. Using Eqs. (2) and (3) and the numerical values given above, the release of He can be predicted assuming a certain value for the permeation energy E_{perm}.

Fig. 5 shows the results obtained using the model above for a permeation energy of 4.0 eV. For comparison, the experimental desorption curve for the highest helium dose (2×10^{16} cm^{-2}) is also shown in Fig. 5. In order to show the effect of
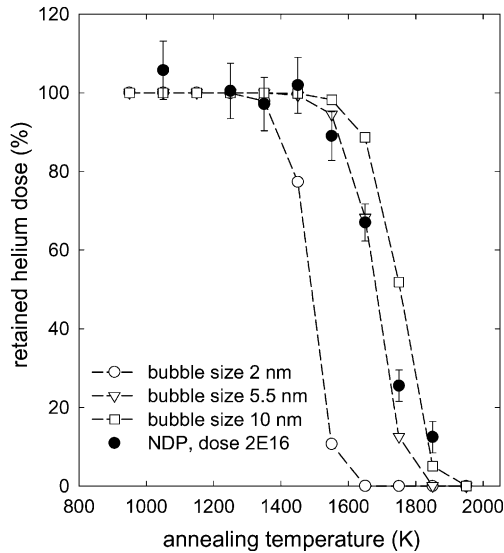
bubble size distribution and, therefore, a different pressure in the bubbles, bubble diameters of 2, 5.5 and 10 nm have been substituted in Eq. (3) with the number of bubbles, N_b fixed to the value given above. When comparing the experimental desorption curve with the theoretical prediction for a bubble size of 5.5 nm (the average size as deduced from the TEM results), the experimental curve falls off slower. Two reasons can be given for this behavior. First, there is a bubble size distribution as observed in Fig. 3. In this case, the desorption is a multi-stage process where helium is first released from high-pressurized small helium bubbles and later from low-pressurized, large helium bubbles. Second, the annealing is a dynamic process during which the average bubble size and the size distribution are changing. At low temperatures, small bubbles are formed that will either dissociate (yielding desorption at low temperature) or agglomerate into large bubbles (yielding desorption at higher temperatures). The fact that the desorption curve of the lowest-dose sample falls of much slower than the curve of the high-dose sample (Fig. 4) indicates that the bubble size distribution is broader in the case of the low-dose sample.

4. Conclusions

At a sufficiently high dose, helium bubbles are formed in He ion implanted Al_2O_3 that reach a maximum volume after annealing at a temperature of 1250 K. TEM observations show that after annealing at this temperature, the bubbles are shaped as discs lying parallel with the surface and that the average bubble size is 5.5 nm for the highest-dose implanted sample (2.0×10^{16} He ions cm^{-2}). At higher temperatures, bubble shrinkage sets in until no bubbles are observed by means of positrons after annealing at 1650 K. This means that the bubbles have shrunk below the size of a few nm. Helium is released from vacancy-type defects in the Al_2O_3 matrix in temperature range of 1650–1850 K, which can be explained by a permeation model combined with a bubble size distribution. The activation energy for permeation is estimated at 4.0 eV.

Fig. 5. Experimental desorption curve (black symbols) for the high-dose (2×10^{16} He cm^{-2}) implanted sample. Added are the desorption curves (open symbols) as obtained using the permeation model (Eq. (2)) with a permeation energy of 4.0 eV.

References

[1] N. Cocuaud, E. Picard, R.J.M. Konings, A. Conti, H. Matzke, Proc. Global 97 (1997) 1044.

[2] C.W. White, C.J. McHargue, P.S. Sklad, L.A. Boatner, G.C. Farlow, Mater. Sci. Reports 4 (1989) 41.

[3] C.W. White, J.D. Budai, S.P. Withrow, J.G. Zhu, E. Sonder, R.A. Zuhr, A. Meldrum, D.M. Hembree Jr., D.O. Henderson, S. Prawer, Nucl. Instr. and Meth. B 141 (1998) 228.

[4] M.D. Rechtin, Radiat. Eff. 42 (1979) 129.

[5] W.R. Allen, S.J. Zinkle, J. Nucl. Mater. 191–194 (1992) 625.

[6] N. Sasajima, T. Matsui, S. Furuno, K. Hojou, H. Otsu, Nucl. Instr. and Meth. B 148 (1999) 745.

[7] H. Schut, A. van Veen, F. Labohm, A.V. Fedorov, E.A.C. Neeft, R.J.M. Konings, Nucl. Instr. and Meth. B 147 (1999) 212.

[8] A. van Veen, H. Schut, P.E. Mijnarends, in: P. Coleman (Ed.), Positron Beams and their Applications, World Scientific, Singapore, 2000, p. 191.

[9] R.G. Downing, G.P. Lamaze, Neutron News 4 (1) (1993) 15.

[10] B.J. Kooi, A. van Veen, J.Th.M. de Hosson, H. Schut, A.V. Fedorov, F. Labohm, Appl. Phys. Lett. 76 (9) (2000) 1110.

[11] R.A. Hakvoort, A. van Veen, P.E. Mijnarends, H. Schut, Appl. Surf. Sci. 85 (1995) 271.

[12] S.W.H. Eijt, C.V. Falub, A. van Veen, H. Schut, P.E. Mijnarends, M.A. van Huis, A.V. Fedorov, Mater. Res. Soc. Symp. Proc. 647 (2001) O14.11.

[13] S.J. Zinkle, C. Kinoshita, J. Nucl. Mater. 251 (1997) 200.

[14] A. van Veen, H. Schut, A.V. Fedorov, F. Labohm, E.A.C. Neeft, R.J.M. Konings, Nucl. Instr. and Meth. B 148 (1999) 768.

[15] A. van Veen, in: S.E. Donnelly, J.H. Evans (Eds.), Fundamental Aspects of inert Gases in Solids, NATO ASI Series B: Physics, 278, Plenum Press, New York, 1991, p. 41.

[16] G. Busker, M.A. van Huis, R.W. Grimes, A. van Veen, Nucl. Instr. and Meth. B 171 (2000) 528.

[17] S. Godey, E. Ntsoenzok, T. Sauvage, A. van Veen, F. Labohm, M.F. Beaufort, J.F. Barbot, Mater. Sci. Eng. 73 (1–3) (2000) 54.